Finite-element modeling of extraordinary magnetoresistance in thin film semiconductors with metallic inclusions

J. Moussa,[1] L. R. Ram-Mohan,[1,2] J. Sullivan,[2] T. Zhou,[3] D. R. Hines,[3] and S. A. Solin[3]
[1]*Quantum Semiconductor Algorithms, Inc., Northborough, Massachusetts 01532*
[2]*Worcester Polytechnic Institute, Worcester, Massachusetts 01609*
[3]*NEC Research Institute, 4 Independence Way, Princeton, New Jersey 08540*
(Received 8 March 2001; published 17 October 2001)

Using finite element analysis, the room temperature extraordinary magnetoresistance recently reported for a modified van der Pauw disk of InSb with a concentric embedded Au inhomogeneity has been calculated, using no adjustable parameters, as a function of the applied magnetic field and the size/geometry of the inhomogeneity. The finite element results are nearly identical to exact analytic results and are in excellent agreement with the corresponding experimental measurements. Moreover, several important properties of the composite InSb/Au system such as the field dependence of the current flow and of the potential on the disk periphery have been deduced. It is found that both the EMR and output voltage depend sensitively on the placement and size of the current and voltage ports.

DOI: 10.1103/PhysRevB.64.184410 PACS number(s): 72.20.My, 72.80.Ey, 72.80.Tm

I. INTRODUCTION

It has been shown experimentally[1,2] that semiconductor thin films with metallic inclusions display extraordinary magnetoresistance (EMR) at room temperature, with enhancements as high as 100–750 000 % at magnetic fields ranging from 0.05 to 4 T. The magnetoresistance (MR) is defined as $\mathrm{MR}=[R(H)-R(0)]/R(0)$, where $R(H)$ is the resistance at finite field H. The experiments were initially performed on a composite van der Pauw disk of a semiconductor matrix with an embedded metallic circular inhomogeneity that was concentric with the semiconductor disk. A similar enhancement has been reported[3] for a rectangular semiconductor wafer with a metallic shunt on one side. While the rectangular geometry with four contacts can be shown to be derivable from the circular geometry by a conformal mapping,[4] the use of a metallic shunt had not been considered earlier.

Magnetic materials and artificially layered metals exhibit giant magnetoresistance (GMR) and manganite perovskites show colossal magnetoresistance (CMR). However, patterned nonmagnetic InSb shows a much larger geometrically enhanced extraordinary MR even at room temperature.

In Fig. 1(a), the typical Hall bar configuration is shown. In an applied magnetic field the electrons have a circular trajectory around the lines of the magnetic field, as displayed in Fig. 1(b). As soon as the current begins to flow, the space charge accumulation on one side gives rise to a (Hall) electric field E_y which is measured through the voltage difference across the Hall bar, the Hall voltage. If we assume only one type of carrier with a Δ-function velocity distribution, the force on the carriers from the Hall field cancels the Lorentz force and the direct current j_x continues to remain the same, as indicated in Fig. 1(c). There is then no magnetic field dependence of the resistance in this case, e.g., the MR, $\Delta\rho/\rho_0=0$ where ρ is the resistivity and ρ_0 is the zero field resistivity.

In the Corbino disk, illustrated in Fig. 2, we have two concentric contacts with the current entering at $r=0$ and exiting at the periphery. In the presence of a magnetic field perpendicular to the Corbino disk the electron trajectories follow circular paths and the resistance is a function of the magnetic field. Moreover, because the conducting electrodes are in this case equipotential surfaces, no space charge accumulates on them and no Hall voltage is developed. Since there is no Hall field to produce a force that competes with the Lorentz force there can be a large MR, which in this case is $\Delta\rho/\rho_0=(\mu H)^2$ where μ is the carrier mobility and H is the applied magnetic field. The geometric differences in the standard Hall geometry and the Corbino geometry yield a significant field dependence of the resistance in the latter. We show here how such geometric effects can be generally exploited to enhance MR.

An additional feature that we wish to employ for obtaining enhanced magnetoresistance is the following. In the presence of metallic inhomogeneities the narrow-gap semiconductors show marked enhancement of the MR. Because of their small carrier masses the narrow gap high mobility semiconductors such as InSb and HgCdTe are the preferred materials to consider. Let us suppose that we have a semiconducting slab with a cylindrical metal (Au) embedded in it, as shown in Fig. 3(a). Suppose that the conductivities of the semiconductor and the metal are σ_S and σ_M, respectively, in the absence of a magnetic field. In low magnetic fields, the current flowing through the material is focused into metallic regions with the metal acting as a short circuit; the current density $\mathbf{j}$ is parallel to the local electric field $\mathbf{E}_{\mathrm{loc}}$ as indicated in Fig. 3(b). Note that for $\sigma_M \gg \sigma_S$ the surface of the metal is essentially an equipotential. Thus $\mathbf{E}_{\mathrm{loc}}$ is normal to the interface between the metal and semiconductor. At finite magnetic field, the current deflection due to the Lorentz force results in a directional difference between $\mathbf{j}$ and $\mathbf{E}_{\mathrm{loc}}$, the angle between them being the Hall angle. For sufficiently high fields the Hall angle approaches 90° in which case $\mathbf{j}$ is parallel to the semiconductor-metal interface and the current is deflected around the metal which acts like an open circuit

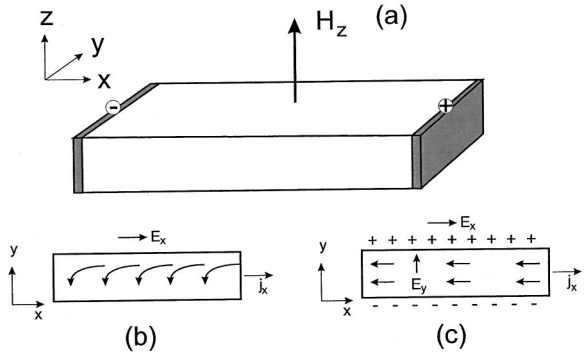

FIG. 1. The Hall configuration: the electron trajectories in a rectangular sample, shown in (a), bend in a magnetic field so that negative charges accumulate at the edge of the *xy* plane, as shown in (b). In the steady state, shown in (c), this leads to an electric field E_y, the Hall field, perpendicular to the longitudinal direction in which the current j_x is flowing. This does not give a magnetic field dependent conductivity.

as indicated in Fig. 3(c). The transition of the metal from a short circuit at low field to an open circuit at high field gives rise to the very large MR or EMR which has been reported by Solin *et al.*[1]

Under steady state conditions the problem of determining the current and the field in the inhomogeneous semiconductor reduces to the solution of Laplace's equation for the electrostatic potential. For some simple structures this problem can be solved analytically.[5] In general, however, the location and material properties of the inhomogeneities can be altered and the semiconducting material can be shaped to enhance the MR. In order to have this freedom to explore the geometrical enhancement of the MR in the device and to be able to consider semiconductor films and metallic inclusions/shunts of arbitrary shape, we require a numerical approach to the simulation of the enhanced MR. In this paper we show that the finite element method is ideally suited to this modeling and demonstrate that the modeling agrees very well with the experiments with no adjustable parameters.

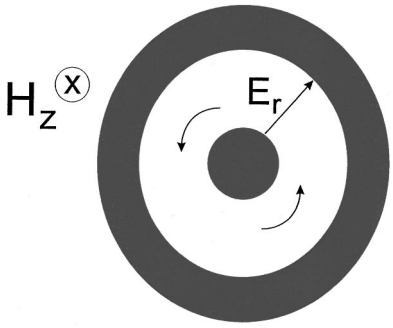

FIG. 2. In the Corbino geometry, the electrodes are concentric with a radial current flowing in the absence of a magnetic field. With a magnetic field present, the electron drift velocity is in the tangential (to the circular region) direction. This leads to a magnetic field dependent conductivity that is geometry dependent. The magnetoresistance $\Delta\rho/\rho_0$ is proportional to H^2 at low field.

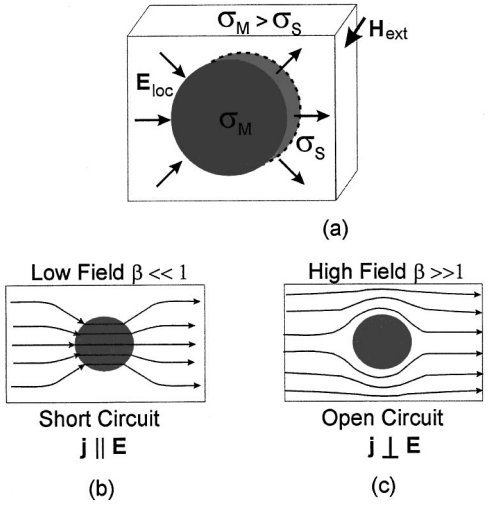

FIG. 3. (a) The extraordinary magnetoresistance (EMR) is manifested by the effect on the boundary conditions at the metal-semiconductor interface as a function of the magnetic field H. (b) At low magnetic fields ($\beta \ll 1$), the current density *j* is parallel to the electric field *E* and the metal acts as a short circuit. (c) At high fields, ($\beta \gg 1$), the system acts as an open circuit.

II. FINITE ELEMENT ANALYSIS OF THE MODIFIED VAN DER PAUW DISK

For the sake of a simple presentation, and for comparison with experiments, we will first consider a circular disk of InSb of thickness *t* containing a concentric disk of Au, with four contacts, or ports as we refer to them, attached symmetrically to the periphery of the semiconductor (see Fig. 4).

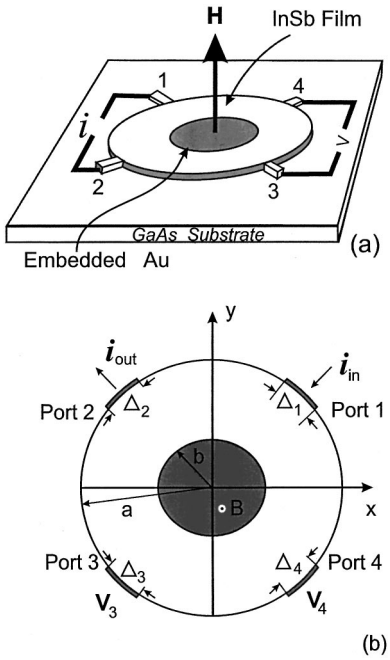

FIG. 4. (a) Circular van der Pauw geometry showing the symmetrically placed contacts and a concentric Au inclusion in a circular InSb sample. (b) The geometry of the structure and the ports (contacts) are shown.

This configuration is called the modified van der Pauw geometry and was first studied analytically by Wolfe and Stillman.[6] The disk of InSb has a radius a while the Au inclusion has a radius b, with the ratio of the radii denoted by $\alpha = b/a$. A current enters port 1 and exits via port 2. The response of the semiconducting disk is measured by the voltage difference between ports 3 and 4. The widths of the ports have been labeled as Δ_i. The disk geometry reduces the problem to a two-dimensional one.

The constitutive relation between the current j and the electric field **E** in the presence of an external magnetic field **H** along the z axis is given by

$$j_i = \sigma_{ij}(H) E_j, \tag{1}$$

where

$$\sigma_{ij}(H) = \frac{\sigma(0)}{1+\beta^2} \begin{bmatrix} 1 & -\beta & 0 \\ \beta & 1 & 0 \\ 0 & 0 & 1 \end{bmatrix} \tag{2}$$

with

$$\beta = \mu H, \tag{3}$$

where μ is again the mobility of the carriers as noted above. The conductivity is given by

$$\sigma(0) = \frac{ne^2\tau}{m^*} = ne\mu = \sigma, \tag{4}$$

where n is the carrier density, m^* is the effective mass, e is the electronic charge, and τ is the collision time. Using Eqs. (3) and (4) the components of the magnetoconductivity tensor can be written explicitly as $\sigma_{xx}(H) = \sigma_{yy}(H) = \sigma/(1+\beta^2)$, $\sigma_{yx}(H) = -\sigma_{xy}(H) = \sigma\beta/(1+\beta^2)$, $\sigma_{zz}(H) = \sigma$ with the remaining components $= 0$.

In the steady state, we have

$$\frac{\partial}{\partial x_i} j_i = 0. \tag{5}$$

With $E_i = -\partial_i \phi$, the electrostatic potential $\phi(x,y)$ satisfies the differential equation

$$\dot{\partial}_i [\sigma_{ij} \partial_j \phi(x,y)] = 0. \tag{6}$$

The boundary conditions at the outer edge at radius $r = a$ are as follows.

(a) At Port 1:

$$(\mathbf{j} \cdot \hat{n}) = -J_{\text{in}} = -\frac{I_{\text{in}}}{\Delta_1 t}. \tag{7}$$

(b) At Port 2:

$$(\mathbf{j} \cdot \hat{n}) = +J_{\text{out}} = \frac{I_{\text{out}}}{\Delta_2 t}. \tag{8}$$

Here, $I_{\text{in}} = I_{\text{out}}$, from current conservation. The quantities j_{in} and j_{out} are positive and their signs have been entered explicitly in the above.

(c) At Ports 3, 4: we have $\phi = V_3$ and $\phi = V_4$, respectively, where these potentials have to be determined by the calculations. The entire width of each port is considered to be at the same voltage.

(d) Along the rest of the semiconductor disk's edge we set $\mathbf{j} = 0$ along the periphery.

(e) Finally, along the metal-semiconductor interface at $r = b$ the normal currents are equal. Hence we have

$$[\sigma_{ij}^{(1)} \partial_j \phi(r=b)](\hat{n}_r)_i = [\sigma_{ij}^{(2)} \partial_j \phi(r=b)](\hat{n}_r)_i \tag{9}$$

or

$$(\mathbf{j} \cdot \hat{n}_r)|_{r=b^-} = (\mathbf{j} \cdot \hat{n}_r)|_{r=b^+}. \tag{10}$$

Here the material index on the conductivity tensor refers to the semiconductor (index $= 1$) and to the metal (index $= 2$).

Rather than directly solving Eq. (6), we begin by setting up the action integral that gives rise to it. This is done in order that we may employ the finite element method.[7] The action integral is given by

$$A = \frac{1}{2} \int \int dx\, dy [\partial_i \phi(x,y)] \sigma_{ij} [\partial_j \phi(x,y)] + \int_{\Delta_1} dl [\phi(x,y)]|_{\Delta_1} j_{\text{in}} - \int_{\Delta_2} dl [\phi(x,y)]|_{\Delta_2} j_{\text{out}}. \tag{11}$$

The double integral in Eq. (11) is just the electrostatic energy in the system. It is instructive to apply the principle of least action to the above equation in order to verify that the variation of the action with respect to the potential function indeed reproduces Eq. (6). Setting the variation of A with respect to the potential function $\phi(x,y)$ to zero we obtain

$$\delta A = 0 = \left[-\int \int dx\, dy\, \delta\phi \{\partial_i \sigma_{ij} [\partial_j \phi(x,y)]\} + \int_{\Gamma(r=a)} dl\, \delta\phi \hat{n} \cdot [\sigma_{ij} (\partial_j \phi)] \right] + \int_{\Delta_1} dl\, \delta\phi j_{\text{in}} - \int_{\Delta_2} dl\, \delta\phi j_{\text{out}}. \tag{12}$$

An integration by parts has been performed in order to obtain the terms in the square brackets. The variations $\delta\phi$ are arbitrary. We therefore choose them as follows.

(i) Choose variations such that $\delta\phi = 0$ on the periphery $r = a$. We then obtain the differential equation, Eq. (6), from the double integral in Eq. (12).

(ii) Now let $\delta\phi = 0$ inside the physical region *and also along the periphery* Δ_i *except at the input port along* Δ_1 where it is chosen to be 1. Then $\delta A = 0$ requires

$$\int_{\Delta_1} dl (j_{\text{in}} + \hat{n} \cdot \mathbf{j}) = 0.$$

In other words, we have $(\hat{n} \cdot \mathbf{j})_{\Delta_1} = -j_{\text{in}}$. This is just Eq. (7).

(iii) Next, choose $\delta\phi = 1$ along Δ_2 and zero elsewhere. Then

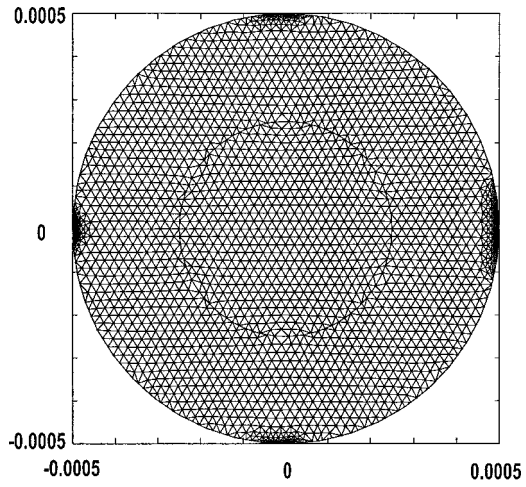

FIG. 5. The discretization of the physical region for $\alpha = b/a = \frac{8}{16}$. The mesh has been made finer in the vicinity of the ports (contacts). The algebraic integer method was used for the mesh generation.

$$\int_{\Delta_2} dl(-j_{\text{out}} + \hat{n}\cdot\mathbf{j}) = 0,$$

implying that $(\hat{n}\cdot\mathbf{j})_{\Delta_2} = j_{\text{out}}$, as in Eq. (8).

(iv) Finally, put $\delta\phi = 0$ in the interior and along Δ_1 and Δ_2. Then $\delta A = 0$ requires that $(\hat{n}\cdot\mathbf{j})_{r=a} = 0$ on the rest of the circular periphery of the semiconductor.

We have shown that our starting action integral with the surface terms for the currents, through the principle of least action, leads to the original differential equation with its boundary conditions including the ''derivative'' boundary conditions on the input and output currents. This procedure is similar to that discussed in Courant and Hilbert[8] for derivative boundary conditions. We now employ the above action in numerical modeling.

In the finite element method, we begin by discretizing the action integral itself. We break up the physical region into triangles, or elements, in each of which the physics of the problem holds. This discretization is performed using an unstructured triangular mesh that is generated by the so-called algebraic integer method.[9] The result of this meshing is shown in Fig. 5. In each of the triangular elements we represent the function $\phi(x,y)$ in terms of local interpolation polynomials $N_i(x,y)$. Each triangle has either three nodes, located at the three vertices of the triangle, or six nodes located at the midpoints of the sides of the triangle and at the vertices.

Let

$$\phi(x,y) = \sum_i \phi_i N_i(x,y), \tag{13}$$

where N_i are unity at node i. The interpolation polynomials are linear for the three-nodal triangle, and quadratic polynomials in x and y in the case of a six-nodal triangle. Using the above functional form in the action integral we integrate out the spatial dependence and express the action in each element [i.e., Eq. (11) limited to the elemental area] in the form

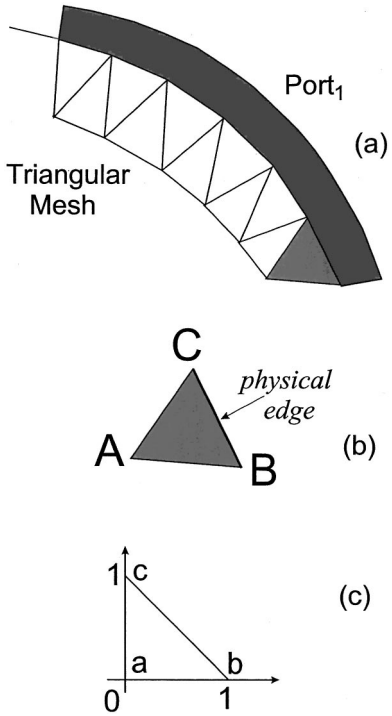

FIG. 6. (a) One edge-triangle from the triangulated physical region near port 1 is highlighted. (b) The selected triangle *ABC* is shown. (c) The edge-triangle is mapped onto a standard right triangle for computation of the action integrals.

$$A^{(\text{ielem})} = \tfrac{1}{2}\,\phi_i M_{ij}^{(\text{ielem})} \phi_j\,. \tag{14}$$

Next, for continuity at the nodes, we add all the contributions from each element by setting the nodal values to be the same for all triangles having a common node. This amounts to an overlay of each element matrix $M_{ij}^{(\text{telem})}$ into a global matrix such that we add the nodal contributions from all triangles having that node in common. We then obtain

$$A = \frac{1}{2}\phi_\alpha M_{\alpha\beta}\phi_\beta + \int_{\Delta_1} dl[\,\phi(x,y)]|_{\Delta_1} j_{\text{in}} - \int_{\Delta_2} dl[\,\phi(x,y)]|_{\Delta_2} j_{\text{out}}\,. \tag{15}$$

The integrals in Eq. (15), that may be designated as ''surface'' terms, need further elaboration. If we assume a constant linear current density across the port the surface terms are readily evaluated as follows. In Fig. 6(a), we show the edge of the physical region along port 1. We have to integrate along the port in order to evaluate the first contour integral in Eq. (15). Consider one of the triangles with one edge coinciding with the contour at port 1. The physical edge is along the side *BC* of the triangle *ABC* of Fig. 6(b). We map this on to a ''standard'' right-angled triangle *abc* of Fig. 6(c). If side *BC* corresponds to side *ab* of the standard triangle, we have

$$\int_B^C dl\ \phi(x,y) j_{\rm in} = j_{\rm in} \int_a^b d\xi \frac{dl}{d\xi} \sum_i \ \phi_i N_i(\xi, o)$$

$$= \tfrac{1}{2}\, l(\phi_C + \phi_B) j_{\rm in}. \qquad (16)$$

Here l is the length of the edge BC. The same result obtains if the side BC corresponds to the side ac of the standard triangle. In the case where the side BC corresponds to the hypotenuse bc of the standard triangle we obtain

$$\int_B^C dl\, \phi(x,y) j_{\rm in} = j_{\rm in} \int_b^c d\lambda \frac{dl}{d\lambda} \sum_i \ \phi_i N_i(\xi, \eta = 1-\xi). \qquad (17)$$

Here

$$d\lambda = \sqrt{(d\xi)^2 + (d\eta)^2} = d\xi \sqrt{1 + \left(\frac{d}{d\xi}(1-\xi)\right)^2} = \sqrt{2}\, d\xi$$

and

$$\frac{dl}{d\lambda} = \frac{l}{\sqrt{2}},$$

so that again Eq. (17) reduces to the right side of Eq. (16). The above calculations can be performed for quadratic interpolation functions when these are employed in representing the potential over each triangle. We thus have an expression for the discretized action given by

$$A = \frac{1}{2}\phi_\alpha M_{\alpha\beta}\phi_\beta + j_{\rm in}\left[\sum_{\substack{\text{edge}\\ \text{sides}\\ \text{on } \Delta_1}} l_i \left\{\frac{1}{6}\phi_1^{(i)} + \frac{2}{3}\phi_2^{(i)} + \frac{1}{6}\phi_3^{(i)}\right\}\right]$$

$$- j_{\rm out}\left[\sum_{\substack{\text{edge}\\ \text{sides}\\ \text{on } \Delta_2}} l_i \left\{\frac{1}{6}\phi_1^{(i)} + \frac{2}{3}\phi_2^{(i)} + \frac{1}{6}\phi_3^{(i)}\right\}\right]. \qquad (18)$$

Now our variational principle is implemented by varying the discretized action A of Eq. (18) with respect to the nodal variables ϕ_α. We obtain

$$\frac{\delta A}{\delta \phi_\alpha} = 0 = M_{\alpha\beta}\phi_\beta + C_i j_{\rm in}\delta_{i\alpha} - C_j j_{\rm out}\delta_{j\alpha}. \qquad (19)$$

Here C_i and C_j are constants determined by evaluating the surface terms as described above. We then have a set of simultaneous equations for the nodal variables ϕ_α.

Due to the connectivity of the triangular mesh the resulting coefficient matrix is sparsely occupied. We first perform a bandwidth reduction of the matrix and then decompose it into the standard **LU** form for Gauss elimination.[10]

We also equate all the nodal values for nodes appearing in ports 3 and 4 in order to define a unique potential at the ports over the lengths Δ_3 and Δ_4. Since no absolute potential values are set in the problem, we assign one of the ports to have zero potential with respect to which all other potentials are measured. The solution of the simultaneous equations now provides us with a unique solution.

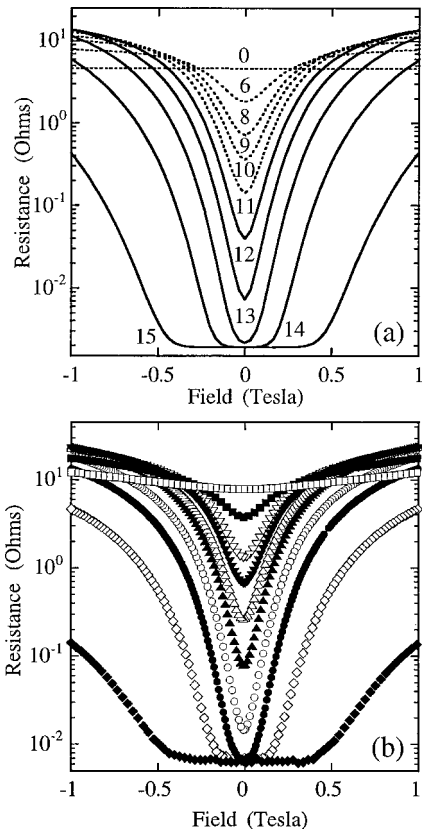

FIG. 7. A plot of the resistance as a function of the magnetic field for $\alpha' = 16(b/a)$ ranging from 0 to 15, as obtained from (a) finite element method calculations and (b) directly from experiments. The symbols in (b) correspond to the following values of $\alpha' :=$ 0—□, 6—■, 8—▽, 9—▼, 10—△, 11—▲, 12—○, 13—●, 14—◇, 15—◆.

III. COMPARISON WITH EXPERIMENTAL RESULTS

The principle quantity of interest is the field and geometry dependence of the effective resistance $R_{mn}(H,\alpha) = [\Delta V_{mn}(H,\alpha)]/i$, where $\Delta V_{mn}(H,\alpha) = V_m(H,\alpha) - V_n(H,\alpha)$, n and m define the voltage ports, i is a constant current and as before $\alpha = b/a$ [see Figs. 4(a) and 4(b)]. Once the effective resistance is known, the EMR can be readily determined from

$$\mathrm{EMR}_{mn}(H,\alpha) = \left(\frac{R_{mn}(H,\alpha) - R_{mn}(0,\alpha)}{R_{mn}(0,\alpha)}\right). \qquad (20)$$

The effective resistance $R_{43}(H,\alpha)$ (see Fig. 4), is plotted in Fig. 7(a) using the parameters for InSb and Au specified in Table I (with values for Cu shown for reference) corresponding to experimental measurements to be described below. Thus the influence of the metallic inhomogeneity is determined by varying the radius of the inner metallic region to change the ratio α. Note that for $\alpha > 13/16$ $R_{43}(H,\alpha)$ is very small and field independent up to an onset field above which it increases very rapidly. This diodelike behavior may offer the opportunity for employing such constructs as a magnetic switch. The physical origin of this diode effect is understood: For a sufficiently large conducting inhomogeneity, deflected

TABLE I. Material parameters used in the calculations.

	Conductivity (300 K) $\sigma\ (\Omega\,\mathrm{m})^{-1}$	Mobility μ $(\mathrm{m}^2/\mathrm{V\,sec})$	Carrier conc. $n\ (\mathrm{m}^{-3})$	Collision time τ (sec)	Effective mass m^*/m_0	Fermi level E_F (eV)
InSb	1.856×10^4	4.55	2.55×10^{22}	3.87×10^{-13}	0.015	
Au	4.52×10^7	5.3×10^{-3}	5.90×10^{28}	3.0×10^{-14}	1.0	5.51
Cu	5.88×10^7	3.34×10^{-3}	8.45×10^{28}	1.9×10^{-14}	1.0	7.0

current will only flow in the correspondingly small annular ring of semiconductor when the field exceeds a critical value. Below that value the current is completely shunted by the inhomogeneity and its path through the semiconductor from the input to the output ports provides a negligible contribution to the resistance.

The calculations of $R_{43}(H,\alpha)$ described above are compared with the corresponding experimental results shown in Fig. 7(b). Those experimental results were obtained from a composite van der Pauw disk of InSb with fourfold symmetric 80 wide current and voltage ports (i.e., $\Delta_i=8°$, $i=1-4$) and an embedded Au inhomogeneity which has been fabricated using methods described in detail elsewhere.[1] The agreement between experiment and the finite element calculation is remarkable in view of the fact that no adjustable parameters were employed in the calculation. The slight shift in the relative values of the abcissae in Figs. 7(a) and 7(b) is probably due to a finite contact resistance between the metal inhomogeneity and the semiconductor which has not been included in the calculation. Moreover, one can notice that the calculated effective resistance for $\alpha=0$ is totally field independent whereas the corresponding experimental result shows a slight field dependence. This difference results from the fact that the physical contribution to the effective resistance from the field dependence of the intrinsic parameters such as the mobility and carrier concentration is small but finite and has not been included in the calculated results.

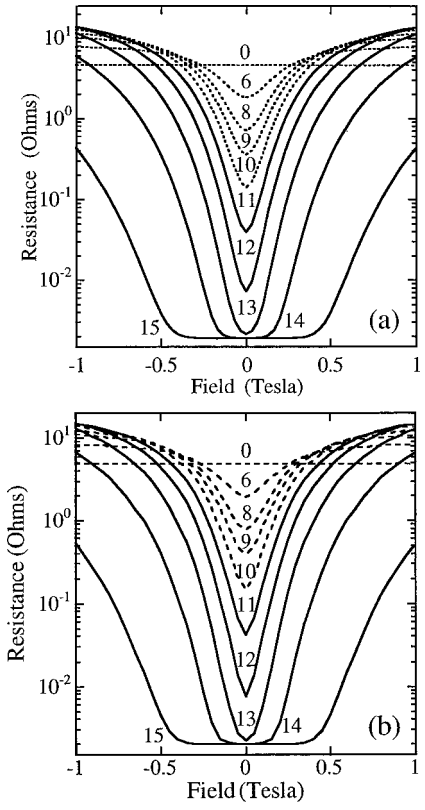

FIG. 8. A plot of the resistance as a function of the magnetic field for $\alpha'=16(b/a)$ ranging from 0 to 15, as obtained from (a) finite element method calculations and (b) analytical calculations.

IV. COMPARISON WITH ANALYTICAL CALCULATIONS

For the highly symmetric centered van der Pauw structure shown in Fig. 4 one can analytically compute the magnetotransport properties as has been described in detail for the low field region ($H<0.1$ T) elsewhere.[5] It is useful to compare the analytic results in the both the low and high field range ($0\leqslant H\leqslant 1$ T) with the finite element method discussed above. The analytic solution for the resistance of the centered van der Pauw structure shown in Fig. 4 with four identical ports of width Δ is[5]

$$\Delta V_{43}(\alpha,\gamma,\eta,\beta,\sigma_0,\phi,t,\theta) = \frac{1+\beta^2}{\sigma_0}\frac{i}{\pi t\Delta}\sum_{n=1}^{\infty}\frac{1}{n^2}\frac{1}{J^2+K^2}\{[(JU-KW)(1-\alpha^{2n}\gamma) - \alpha^{2n}\eta(KU+JW)]\cos(n\theta)+[(KU+JW) \times(1-\alpha^{2n}\gamma)+\alpha^{2n}\eta(JU-KW)]\sin(n\theta)\}, \quad (21)$$

where

$$J=1+\alpha^{2n}\gamma+\beta\alpha^{2n}\eta,$$

$$K=\beta+\alpha^{2n}\eta-\beta\alpha^{2n}\gamma,$$

$$U=\sin(n\pi/2+n\Delta/2)-\sin(n\pi/2-n\Delta/2)-2\sin(n\Delta/2),$$

$$W=\cos(n\pi/2-n\Delta/2)-\cos(n\pi/2+n\Delta/2), \quad (22)$$

$$\gamma=[(\omega_0^2-\omega^2)+(\omega_0\beta_0-\omega\beta)^2]/[(\omega_0+\omega)^2+(\omega_0\beta_0-\omega\beta)^2],$$

$$\eta=[2\omega(\omega_0\beta_0-\omega\beta]/[(\omega_0+\omega)^2+(\omega_0\beta_0-\omega\beta)^2],$$

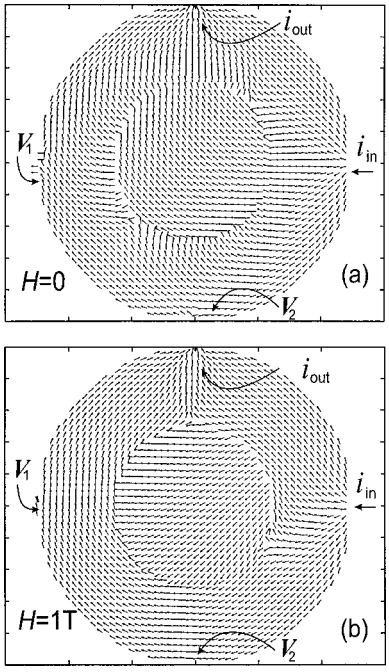

FIG. 9. The current flow in the van der Pauw geometry for a circular InSb wafer with a concentric metallic inhomogeneity and $\alpha' = 16(b/a) = 8$, (a) at $H = 0$ and (b) at $H = 1$ T. The lengths of the arrows are not to scale.

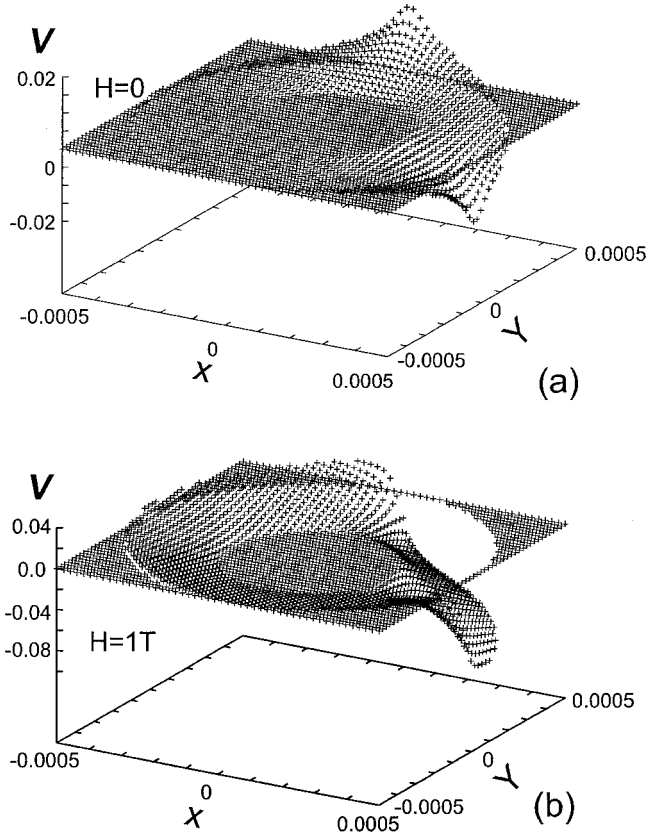

FIG. 10. The potential distribution in the van der Pauw geometry for a steady state current through ports 1 and 2 (a) in the absence of an applied magnetic field and (b) at $H = 1$ T.

while $\beta_0 = \mu_0 H$, $\omega = \sigma/(1+\beta^2)$, $\omega_0 = \sigma_0/(1+\beta_0^2)$, t is the thickness of the disk and μ_0, and σ_0 are the mobility and conductivity of the metal, respectively.

The effective resistance for the configuration shown in Fig. 4 calculated from Eqs. (20)–(22) using no adjustable parameters is compared with the corresponding finite element analysis in Fig. 8. While, the two methods yield nearly identical results, as can be seen from that figure, the finite element method is not restricted to highly symmetric structures such as that shown in Fig. 4.

V. SUMMARY REMARKS AND CONCLUSION

It is clear from the results that the finite element method is able to accurately reproduce the experimental results for $R_{mn}(H,\alpha)$. Indeed, given the solution for the potential $V_m(H,\alpha)$ we can compute not only the EMR [see Eq. (20)] but also a number of other interesting properties of the modified van der Pauw disk. In Fig. 9 we show the flow lines of the current. The arrows indicate the direction of current flow at $H = 0$ and at $H = 1T$. The lengths of the arrows are not to scale in the figure. The effect of the applied magnetic field on the current deflection at the interface between the semiconductor and the inhomogeneity can be readily seen from the figure. The large perturbation to the potential at the current ports caused by the applied field as shown in Fig. 10 for the two cases $H = 0$ and $H = 1$ T for a value of $\alpha = 0.5$ indicates that the EMR will be very sensitive to the position and width of the voltage ports. Indeed, for the modified van der Pauw structure addressed here, the output voltage, $\Delta V_{mn}(H,\alpha)$ decreases as the EMR is increased by the selection of the voltage and current port locations. The current through the structure provides the driving terms in the set of simultaneous equations obtained from the variational principle applied to the discretized action. Here we see that the finite element approach is able to capture the important dependence of the response of the structure to the geometrical placement and location of the current ports.

We have demonstrated an advantage of the action integral formulation of the finite element analysis in its ability to apply the current (derivative) boundary conditions very directly in specific sections of the boundary, i.e., at the current ports, while allowing the values of the potential at other segments of the periphery to be self-consistently determined from the variation of the discretized action integral. The values of the potential at all the nodes located just at the voltage-measuring ports are equated to each other since the voltage is the same across the leads. This is implemented by ''folding in,'' or adding together, of columns of the global matrix generated in the finite element method that correspond to the nodes at the voltage ports. Such details of the boundary conditions can be accounted for with ease within the framework of the finite element method.

Finally note that the use of a bandwidth reducer and sparse matrix LU solvers substantially reduces the computer time for the calculations. With 6000 nodal points in the typical unstructured mesh used in the calculations, we have a 6000×6000 (sparse) matrix that is solved for over 60 values of the magnetic field. The global matrix is evaluated afresh

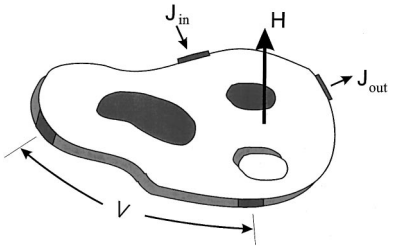

FIG. 11. The four-contact van der Pauw geometry for an arbitrarily shaped InSb thin film with distributed metallic inclusions of arbitrary shape and with a hole in it of arbitrary shape.

each time and calculations for a single curve, for a given value of α, is completed in about 240 s on a 500 MHz Pentium PC running the NT operating system.

The true flexibility and the power of the finite element method comes into its own when the physical semiconductor film is not only of arbitrary shape but contains both filled (conducting) and empty (insulating) embedded inhomogeneities of arbitrary shape as shown schematically in Fig. 11. Given that the EMR discussed here is geometrically enhanced, in the finite element method we now have the means of designing and exploring geometrically more complex heterostructures for additional improvements in the performance of EMR-based magnetic devices *before* they are fabricated for electronic applications.

ACKNOWLEDGMENTS

We wish to thank Quantum Semiconductor Algorithms for the use of their mesh generator ''AimGrid'' and sparse matrix programs ''SMP'' which were employed in the finite element modeling.

[1] S. A. Solin, Tineke Thio, D. R. Hines, and J. J. Hermans, Science **289**, 1530 (2000).

[2] S. A. Solin, Tineke Thio, D. R. Hines, J. J. Heremans, and T. Zhou, *Proceedings of the 25th International Conference on the Physics of Semiconductors*, Osaka, Japan, edited by N. Miura (Springer, Berlin, 2001), pp. 1771-1774.

[3] T. Zhou, D. R. Hines, and S. A. Solin, Appl. Phys. Lett. **78**, 667 (2001).

[4] R. S. Popovic, *Hall Effect Devices* (Adam Hilger, Bristol, 1991).

[5] T. Zhou, S. A. Solin, and D. R. Hines, J. Magn. Magn. Mater. (to be published).

[6] C. M. Wolfe and G. E. Stillman, Appl. Phys. Lett. **18**, 205 (1971); C. M. Wolfe, G. E. Stillman, and J. A. Rossi, J. Electrochem. Soc. **119**, 250 (1972); C. M. Wolfe and G. E. Stillman, in *Semiconductors and Semimetals*, edited by R. K. Willardson and A. C. Beer (Academic, New York, 1975), Vol. 10, p. 175.

[7] O. C. Zienkiewicz and R. L. Taylor, *The Finite Element Method*, 4th ed. (McGraw-Hill, New York, 1994); T. J. R. Hughes, *The Finite Element Method* (Prentice-Hall, Englewood Cliffs, NJ, 1987); L. R. Ram-Mohan, *Finite Element and Boundary Element Applications to Quantum Mechanics* (Oxford University Press, Oxford, in press).

[8] R. Courant and D. Hilbert, *Methods of Mathematical Physics* (Interscience Publishers, New York, 1953).

[9] J. M. Sullivan, in *CAD/CAM Robotics and Factories of the Future*, edited by Birendra Prasad (Springer, Berlin, 1988), Vol. I.

[10] W. H. Press, S. A. Teukolsky, W. T. Vetterling, and B. P. Flannery, *Numerical Recipies in C* (Cambridge University Press, Cambridge, UK, 1992).